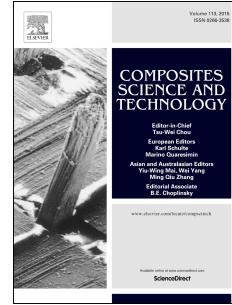


# Journal Pre-proof

Assessment of dynamic mode-I delamination driving force in double cantilever beam tests for fiber-reinforced polymer composite and adhesive materials

Tianyu Chen, Yiding Liu, Christopher M. Harvey, Kun Zhang, Simon Wang, Vadim V. Silberschmidt, Bingchen Wei, Xiang Zhang



PII: S0266-3538(22)00374-8

DOI: <https://doi.org/10.1016/j.compscitech.2022.109632>

Reference: CSTE 109632

To appear in: *Composites Science and Technology*

Received Date: 25 January 2022

Revised Date: 27 May 2022

Accepted Date: 6 July 2022

Please cite this article as: Chen T, Liu Y, Harvey CM, Zhang K, Wang S, Silberschmidt VV, Wei B, Zhang X, Assessment of dynamic mode-I delamination driving force in double cantilever beam tests for fiber-reinforced polymer composite and adhesive materials, *Composites Science and Technology* (2022), doi: <https://doi.org/10.1016/j.compscitech.2022.109632>.

This is a PDF file of an article that has undergone enhancements after acceptance, such as the addition of a cover page and metadata, and formatting for readability, but it is not yet the definitive version of record. This version will undergo additional copyediting, typesetting and review before it is published in its final form, but we are providing this version to give early visibility of the article. Please note that, during the production process, errors may be discovered which could affect the content, and all legal disclaimers that apply to the journal pertain.

© 2022 Published by Elsevier Ltd.

**Author Contributions:**

**Tianyu Chen:** Conceptualization, Methodology, Formal analysis, Writing-Original Draft

**Yiding Liu:** Conceptualization, Validation, Investigation, Data Curation

**Christopher M. Harvey:** Methodology, Formal analysis, Writing-Review&Editing

**Kun Zhang:** Visualization, Resources, Funding acquisition, Writing-Original Draft

**Simon Wang:** Methodology, Visualization, Writing-Review&Editing

**Vadim V. Silberschmidt:** Writing-Review&Editing, Supervision

**Bingchen Wei:** Project administration, Resources, Funding acquisition

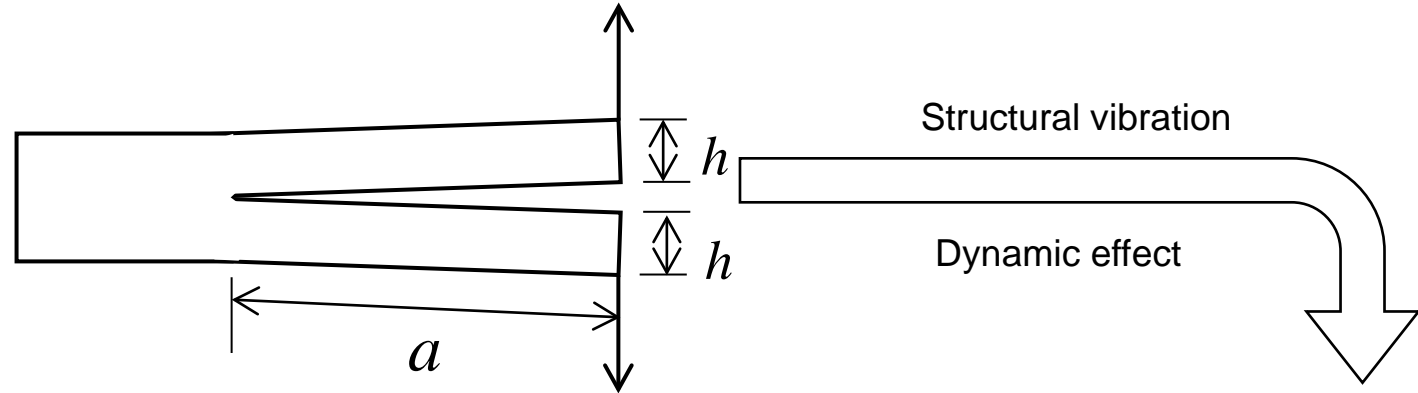
**Xiang Zhang:** Visualization, Supervision, Writing-Review&Editing

All authors have read and agreed to the published version of the manuscript.

Journal Pre-proof

# Assessment of dynamic mode-I delamination driving force in double cantilever beam tests

$$w_0(t) = w_1 + \sum_{n=1}^N c_n t^n + \sum_{m=1}^M d_m \sin(\theta_m t)$$



$$w_0(t) = w_1 + \sum_{n=1}^N c_n t^n + \sum_{m=1}^M d_m \sin(\theta_m t)$$

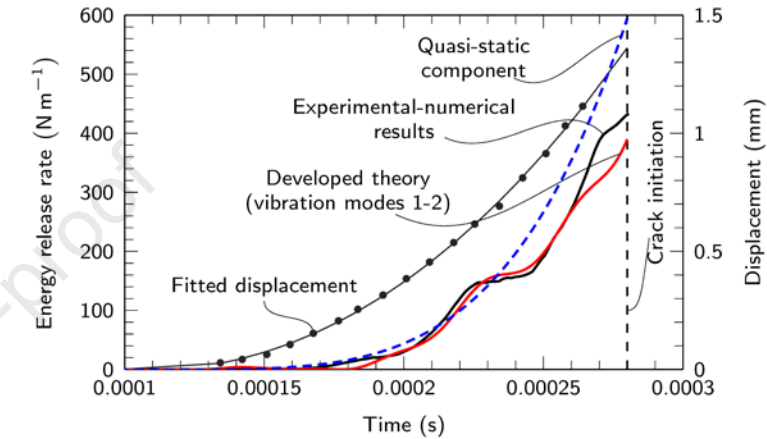
## Analytical solution

**General displacement**  
a combination of quasi-static, dynamic and cyclic loads

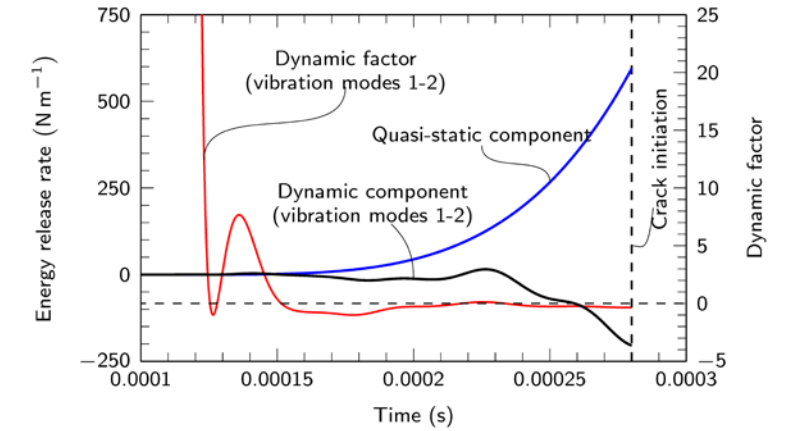
$$G = \frac{EI}{b} \left\{ \begin{array}{l} \frac{2}{a} \sum_{i=1}^{\infty} \left[ \begin{array}{l} -\beta_i^2 \int_0^a \phi_i(x) F_0(x) dx \cos(\omega_i t) \\ -\frac{c_i \beta_i^2}{\omega_i} \int_0^a \phi_i(x) F_1(x) dx \sin(\omega_i t) \\ + \frac{\beta_i^5 \Lambda_i}{\omega_i} \sum_{m=1}^M \frac{\theta_m d_m}{(\beta_i^4 - \gamma_m^4)} \sin(\omega_i t) \end{array} \right] \\ + \frac{3}{a^2} w_1 \\ + F_0^{(2)}(0) + \sum_{n=1}^N F_n^{(2)}(0) c_n t^n \\ - \sum_{m=1}^M \frac{\gamma_m^2 d_m [\sinh(\gamma_m a) + \sin(\gamma_m a)]}{[\sinh(\gamma_m a) \cos(\gamma_m a) - \cosh(\gamma_m a) \sin(\gamma_m a)]} \sin(\theta_m t) \end{array} \right\}^2$$

## Applications

Split Hopkinson bar impact

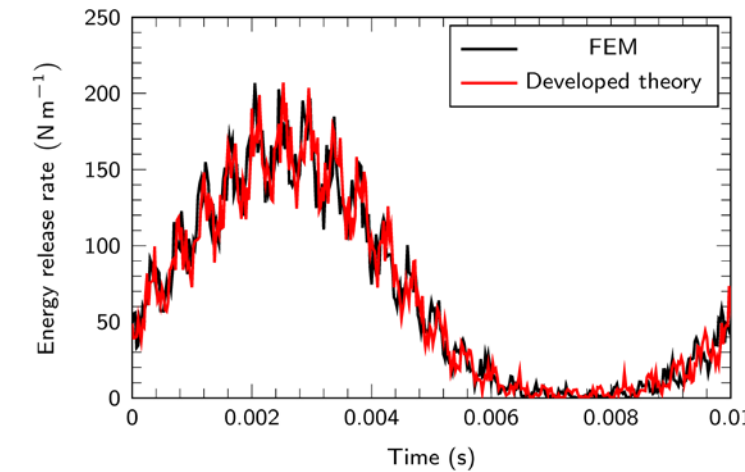


Total energy release rate (ERR)

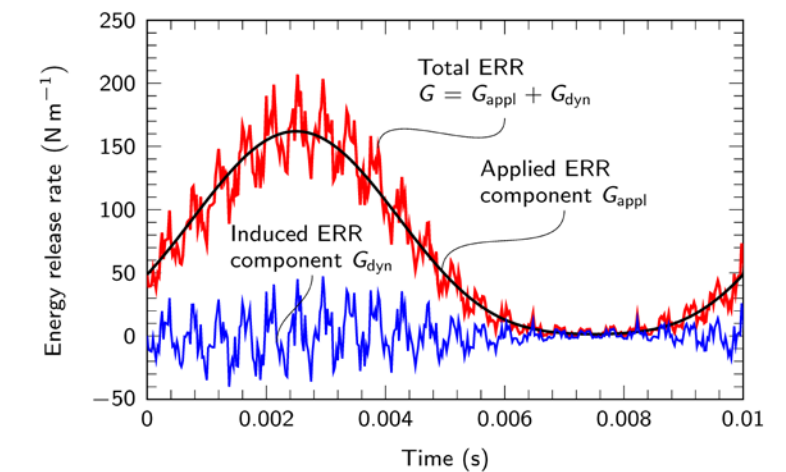


ERR partition and dynamic factor

Cyclic loads



Total ERR



ERR partition

1 **Assessment of dynamic mode-I delamination driving force in double cantilever beam**  
 2 **tests for fiber-reinforced polymer composite and adhesive materials**

3 Tianyu Chen<sup>a</sup>, Yiding Liu<sup>b</sup>, Christopher M. Harvey<sup>c,d</sup>, Kun Zhang<sup>a,e,\*</sup>, Simon Wang<sup>c,d</sup>, Vadim  
 4 V. Silberschmidt<sup>f</sup>, Bingchen Wei<sup>a,b,g,\*</sup>, Xiang Zhang<sup>h</sup>

5 <sup>a</sup>*Key Laboratory of Microgravity (National Microgravity Laboratory), Institute of Mechanics, Chinese Academy*  
 6 *of Sciences, Beijing 100190, China*

7 <sup>b</sup>*School of Physics, Engineering & Computer Science, University of Hertfordshire, Hatfield, AL10 9AB, UK*

8 <sup>c</sup>*Department of Aeronautical and Automotive Engineering, Loughborough University, Loughborough,*  
 9 *Leicestershire LE11 3TU, UK*

10 <sup>d</sup>*School of Mechanical and Equipment Engineering, Hebei University of Engineering, Handan 056038, China*

11 <sup>e</sup>*School of Engineering Science, University of Chinese Academy of Sciences, Beijing 100049, China*

12 <sup>f</sup>*Wolfson School of Mechanical, Electrical and Manufacturing Engineering, Loughborough University,*  
 13 *Loughborough, Leicestershire LE11 3TU, UK*

14 <sup>g</sup>*Center of Materials Science and Optoelectronics Engineering, University of Chinese Academy of Sciences,*  
 15 *Beijing 100049, China*

16 <sup>h</sup>*Centre for Manufacturing and Materials Engineering, Coventry University, Coventry, CV1 5FB, UK*

---

17 **Abstract**

18 The double cantilever beam (DCB) tests are widely used to assess the interfacial delamination  
 19 properties of laminated composites. For quasi-static loads, the DCB tests are standardized based on the  
 20 beam mechanics; for dynamic loads, however, such as high-loading-rate impact and cyclic loads, there  
 21 is no established analytical theory. This presents a significant obstacle preventing the research  
 22 community from assessing the delamination behavior of composites or adhesives for their application  
 23 under complex in-service loads. In this paper, the theory of evaluating dynamic mode-I delamination  
 24 driving force for DCBs under general displacement loads is developed for the first time, accounting for  
 25 structural vibration effects. The developed theory is demonstrated by two examples: high-loading-rate  
 26 split Hopkinson bar impact and cyclic fatigue loads. The analytical solutions are validated by published  
 27 experiment results and in-house tests. This work provides a fundamental analytical tool to study and  
 28 assess the fracture behavior of fiber reinforced polymer composite and adhesive materials under various  
 29 loading conditions.

30  
 31 **Keywords:** Double cantilever beam test; Dynamic energy release rate; General displacement loads;  
 32 Cyclic loads; High loading rate and impact

---

\* Corresponding Author

Email addresses: chentianyu@imech.ac.cn (Tianyu Chen),  
 zhangkun@imech.ac.cn (Kun Zhang),  
 weibc@imech.ac.cn (Bingchen Wei)

33	<b>Nomenclature</b>	
34	$a$	Delamination length
35	$c_n$	Coefficient of $n$ th polynomial displacement component
36	$d_m$	Magnitude of $m$ th cyclic displacement component
37	$E$	Young's modulus
38	$f$	Frequency of applied cyclic displacement
39	$f_{\text{dyn}}$	Dynamic factor
40	$F_n(x)$	Shifting function for $n$ th polynomial displacement component
41	$G$	Dynamic energy release rate (ERR) as the total ERR
42	$G_{\text{appl}}, G_{\text{dyn}}$	Applied ERR component, ERR component due to dynamic effect
43	$G_{\text{st}}^{\text{U}}$	ERR component due to the strain energy of quasi-static motion
44	$H_m(x)$	Shifting function for $m$ th cyclic displacement component
45	$P(x)$	Shifting function for initial time-independent displacement component
46	$Q(t)$	Induced displacement
47	$R$	Ratio of minimum to maximum applied displacement in cyclic load
48	$T_i(t), \dot{T}_i(t)$	Modal displacement and velocity of $i$ th normal mode
49	$t$	Time
50	$w_0(t)$	Applied general displacement
51	$w_1$	Applied initial time-independent displacement component
52	$w(x,t), w_{\text{fv}}(x,t)$	Deflections for total and free vibration responses
53	$W_i(x)$	$i$ th normal mode
54	$\beta_i$	$i$ th vibration mode's wavenumber
55	$\delta_{ij}$	Kronecker delta
56	$\delta_{\text{max}}, \delta_{\text{min}}$	Applied maximum and minimum cyclic displacement
57	$\theta_m$	Angular frequency of $m$ th applied cyclic displacement component
58	$\nu$	Poisson's ratio
59	$\xi_{\text{range}}, \xi_{\text{mean}}$	Contribution of applied range and mean of displacement
60	$\xi_i$	$i$ th induced vibration contribution
61	$\rho$	Density
62	$\phi_i(x)$	$i$ th mode shape
63	$\chi_i$	Ratio of $\xi_i$ and $\xi_{\text{range}}$
64	$\omega_i$	Angular frequency of $i$ th vibration mode

## 65 1. Introduction

66 Carbon-fiber-reinforced plastics (CFRPs) are widely used in the aerospace, automotive,  
67 civil engineering, energy and other sectors, where the light-weight structures are desired due  
68 to their high specific stiffness and strength [1][2]. Without reinforcement in the transverse  
69 direction, however, CFRPs are prone to delaminate along the interfaces between laminae  
70 [3][4][5]. Many studies focused on the improvement of fracture toughness by toughening the

71 resins/adhesives [6][7] or by using additional transverse reinforcements (stitching [8][9] or z-  
72 pins [10][11]) to improve the delamination-resisting force. To assess the mode-I delamination  
73 behavior and to measure the fracture toughness or fatigue delamination growth rate, usually  
74 double-cantilever beams (DCBs) are employed according to a standardized test method in  
75 ASTM D5528 [12], but this is performed in the quasi-static loading regime. For real  
76 engineering structures, however, for instance, aeronautical components, which are prone to  
77 impact and in-service cyclic loads, the conventional measurement of delamination driving  
78 force, that is, energy release rate (ERR), is not adequate, and further fundamental knowledge  
79 of their fracture behavior under dynamic loads is required [13]. It is worth noting that under  
80 dynamic and cyclic loads, not only the strain energy can be dissipated during delamination  
81 advancement but also the kinetic energy, therefore, the delamination driving force is called  
82 ERR or dynamic ERR rather than strain energy release rate [14][15][16][17]. As noted by  
83 Freund [14], dynamic fracture addresses the fracture phenomena when material inertia  
84 becomes significant, and, therefore, the assessment of delamination driving force must consider  
85 the inertial effect and kinetic energy associated; this driving force is the dynamic ERR. For a  
86 DCB under impact load, the dynamic ERR  $G$  as the total ERR can be partitioned into two  
87 components, namely, the ERR component due to strain energy of quasi-static motion  $G_{st}^U$  and  
88 the ERR component due to dynamic effect  $G_{dyn}$ , where  $G = G_{st}^U + G_{dyn}$ . For a DCB under cyclic  
89 load, the dynamic ERR  $G$  can be partitioned into two components, namely, the applied ERR  
90 component  $G_{appl}$  and the ERR component due to dynamic effect  $G_{dyn}$ , where  $G = G_{appl} + G_{dyn}$ .  
91 This definition is described in Section 2.

92 The assessment of delamination behavior under impact or high loading rates was initially  
93 studied with using a servo-hydraulic machine [18] (with a limited range of high loading rates),  
94 and drop weight impact [19] (which suffers from the issue of mixed-mode loading due to  
95 unsymmetric opening), and more recently, split Hopkinson bar [20][21]. The last method is  
96 more efficient in generation of high-loading rates as well as producing symmetric opening to  
97 assess a pure mode-I delamination behavior. But since there is no theory to guide the  
98 experimental setup and to post-process the experimental data, the researchers [21][22][23] had  
99 to adopt experimental-numerical methods. Usually, the delamination driving force is calculated  
100 with numerical simulations, which require experimental data first, such as the applied  
101 displacement or external force, crack length, and, then, incorporate these data into numerical  
102 models to derive the ERR with respective numerical methods, such as virtual crack-closure  
103 technique (VCCT) or cohesive-zone modelling (CZM). This method lacks transferability that

104 enables one numerical model to be directly adopted to study other cases, since numerical  
105 models are mostly suitable for specific cases, so there is a pragmatic requirement for theoretical  
106 development to resolve this.

107 DCBs under cyclic loads can be used to measure fatigue delamination-initiation toughness  
108 and study fatigue delamination-propagation behavior under cyclic loads. The conventional  
109 method standardized in ASTM D6115 [24], allows the fatigue delamination behavior to be  
110 tested at frequencies only between 1 and 10 Hz [25][26] to avoid heating effects. Also the  
111 solution for the fatigue delamination driving force, that is, maximum strain energy release rate  
112 (rather than maximum ERR) accounts only for quasi-static motion, without considering a  
113 dynamic effect of cyclic loads. Nevertheless, Maillet et al. [27] designed a novel device capable  
114 of applying a frequency of up to 100 Hz with an insignificant temperature rise. For even higher  
115 frequencies, heating effects can be mitigated by cooling [28] or intermittently interrupted  
116 cooling [29]. The assessment of the fatigue delamination driving force in ASTM D6115 [24],  
117 however, still requires measurement of the applied load, but under high-frequency cyclic loads,  
118 the slender DCB structure experiences significant vibration due to inertia. In this case, therefore,  
119 the external force cannot be measured accurately, resulting in an incorrect assessment of  
120 dynamic ERR. To address this, an analytical theory considering the dynamic effect of DCB but  
121 allowing no measurement of external force is desirable, which can be used to investigate the  
122 cyclic-load-induced dynamic effect as well as the frequency effect for fatigue delamination  
123 driving force.

124 As discussed above, the previous literature was focused more on experimental analysis  
125 using experiments at high loading rates, impact and cyclic loads. To the authors' best  
126 knowledge, no analytical model was developed to study the dynamic effect explicitly; therefore,  
127 researchers have to resort to experimental-numerical methods. Accordingly, in this paper, the  
128 theory of dynamic mode-I delamination in a DCBs test is developed for general displacement  
129 loads including high-loading-rate and cyclic ones to provide an analytical solution that can be  
130 employed to study the dynamic effect and to post-process the experimental data for  
131 delamination initiation. The theoretical solutions for the delamination driving force in presence  
132 of structural vibration would allow measurements of the dynamic fracture toughness at  
133 initiation under arbitrary dynamic loads as well as investigations of fatigue delamination  
134 behavior. Note that the delamination propagation under dynamic loads, as a dynamic moving  
135 boundary problem, is beyond the scope of this paper, since it requires consideration of crack-  
136 propagating speeds, the dispersive nature of the beam as 1D waveguide to supply the energy  
137 flux to the crack tip, and the Doppler effect due to the fast-moving crack tip. The interested

138 readers can consider [16]. In this paper, the theory is derived in Section 2 and applied to  
 139 delamination problems under split Hopkinson bar impact and cyclic loads. Validation by  
 140 experiments and verification against numerical models are presented in Section 3. Conclusions  
 141 are given in Section 4.

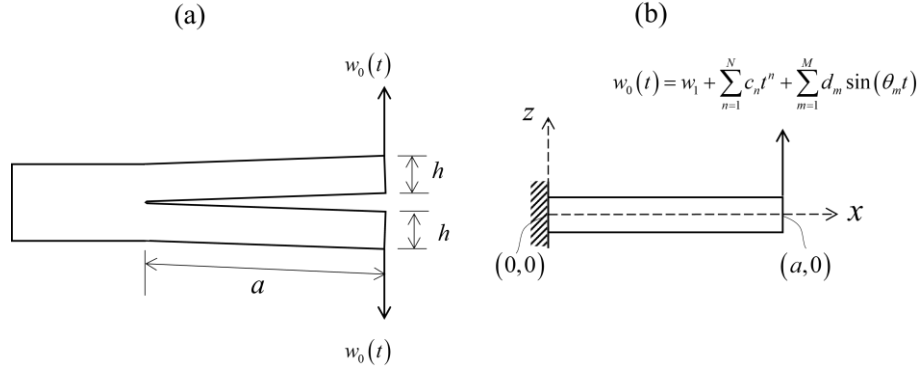
## 142 2. Theory

143 In this section, a theoretical solution for the dynamic ERR of a DCB specimen under general  
 144 displacement loads (as the loading conditions) is derived analytically in the context of structural  
 145 vibration based on beam dynamics. The configuration of the symmetric DCB specimen is  
 146 shown in Fig. 1a: the delamination length is  $a$ , the thickness and width for one DCB arm are  $h$   
 147 and  $b$ , and, therefore, the cross-sectional area is  $A = bh$  and the second moment of area is  
 148  $I = bh^3/12$ . Following the conventional analytical method of analyzing a DCB, the delaminated  
 149 region of the beam is isolated and assigned the coordinates as shown in Fig. 1b, where the crack  
 150 tip is assumed to be built-in at  $x = 0$ , with the deflection of beam section in  $x$ - $z$  plane, denoted  
 151  $w(x, t)$ . Note that in reality the crack tip can rotate, and so the built-in boundary-condition  
 152 assumption does not predict the ERR accurately. This is addressed by introducing the effective  
 153 delamination length  $a_{\text{eff}} = (a + \Delta)$ , as in ASTM D5528 [12] originating in [30], or by  
 154 analytical solution [31]. It is also assumed that  $h \ll a$ , so that the Euler-Bernoulli beam theory  
 155 applies.

156 The general applied time-dependent displacement at the free end is assumed to be of the  
 157 form

$$158 \quad w_0(t) = w_1 + \sum_{n=1}^N c_n t^n + \sum_{m=1}^M d_m \sin(\theta_m t), \quad (1)$$

159 where  $w_1$  is the initial time-independent displacement component,  $\sum_{n=1}^N c_n t^n$  is the time-  
 160 dependent polynomial component, and  $\sum_{m=1}^M d_m \sin(\theta_m t)$  is the harmonic component,  
 161 representing quasi-static, dynamic and cyclic applied displacements, respectively.



162  
 163 Fig. 1. (a) Schematic of DCB specimen; (b) prescribed coordinate system and boundary  
 164 assumption

165 Generally, the ERR of a stationary delamination in a DCB under dynamic loads can be  
 166 determined by the crack-tip bending moments, using a crack-tip energy flux integral [14][16],  
 167 and the dynamic ERR is

$$168 \quad G = 2 \frac{1}{2bE} \frac{\left[ EIw^{(2)}(0,t) \right]^2}{I}, \quad (2)$$

169 where  $EIw^{(2)}(0,t)$  is the internal bending moment of one DCB arm at crack tip  $x = 0$ , with  
 170  $w(x,t)$  being the displacement of this DCB arm (Fig. 1b), and the coefficient of 2 in Eq. (2)  
 171 indicates that the total ERR is for DCB specimen with two DCB arms. Eq. (2) is for the plane-  
 172 stress condition. For the plane-strain condition,  $E$  in Eq. (2) and throughout this paper should  
 173 be replaced with  $E/(1 - \nu^2)$ .

174 The deflection of the DCB arm shown in Fig. 1b is derived in Section 2.1, which is then  
 175 employed to determine the dynamic ERR in Section 2.2 with two important applications for a  
 176 split Hopkinson bar impact in Section 2.2.1 and for a cyclic fatigue load in Section 2.2.2.

## 177 2.1. Dynamic transverse response of DCB arm under general displacement

### 178 2.1.1. Deflection assumptions

179 Under the applied general displacement  $w_0(t)$  given in Eq. (1), the dynamic transverse  
 180 deflections of the DCB arm  $w(x,t)$  can be assumed of the following form by introducing shifting  
 181 functions [32]:

$$182 \quad w(x,t) = P(x)w_1 + w_{iv}(x,t) + F_0(x) + \sum_{n=1}^N F_n(x)c_n t^n + \sum_{m=1}^M H_m(x)d_m \sin(\theta_m t), \quad (3)$$

183

184 where  $P(x)$  is the shifting function for the time-independent initial displacement of  $w_1$ ,  
 185  $w_{fv}(x,t)$  is the free-vibration component, and  $F_n(x)$  and  $H_m(x)$  are the corresponding  
 186 shifting functions for applied polynomial-displacement and harmonic-displacement  
 187 components, respectively. The physical understanding of shifting functions is the distribution  
 188 of the respective applied displacement components along the DCB arm. Particularly for the  
 189 quasi-static component  $w_1$ , it is not time-dependent and, therefore, its contribution can be  
 190 solved within the quasi-static beam mechanics giving  $P(x) = -x^3/(2a^3) + 3x^2/(2a^2)$ . The 0th-  
 191 order shifting function  $F_0(x)$  is time-independent but induced by the time-dependent  
 192 polynomial displacement component according to Grant [32], indicating the nonlinear effects  
 193 of the applied polynomial-displacement component.

194 The governing equations for the free-vibration component  $w_{fv}(x,t)$ , and the shifting  
 195 functions  $F_n(x)$  and  $H_m(x)$ , are now derived (boundary conditions detailed in Appendix A).  
 196 It is worth noting that the boundary conditions for the 0th shifting function are  $F_0(a) = 0$ ,  
 197 different from the other order shifting functions, for which  $F_n(a) = 1$  ( $n \geq 1$ ). The free-  
 198 vibration solution for  $w_{fv}(x,t)$  is given in Section 2.1.2 and the solutions for the shifting  
 199 functions  $F_n(x)$  and  $H_m(x)$  are in Sections 2.1.3 and 2.1.4, respectively.

200 The equation of motion for the Euler-Bernoulli beam [33] in free vibration is

$$201 \quad EIw^{(4)}(x,t) + \rho A \ddot{w}(x,t) = 0. \quad (4)$$

202 By combining Eqs. (3) and (4), and forcing homogeneous conditions, the governing equations  
 203 for the free-vibration component and the shifting functions are derived as

$$204 \quad EIw_{fv}^{(4)}(x,t) + \rho A \ddot{w}_{fv}(x,t) = 0, \quad (5)$$

$$205 \quad EI \sum_{n=1}^N F_n^{(4)}(x) c_n t^n + \rho A \sum_{n=2}^N n(n-1) F_n(x) c_n t^{n-2} = 0, \quad (6)$$

$$206 \quad EI \sum_{m=1}^M H_m^{(4)}(x) - \rho A \sum_{m=1}^M \theta_m^2 H_m(x) = 0. \quad (7)$$

## 207 2.1.2. Solution for free-vibration component

208 By the method of separation of variables, the free-vibration component  $w_{fv}(x, t)$  can be  
 209 expressed as a summation of products of normal mode  $W_i(x)$  and modal displacement  $T_i(t)$ :

$$210 \quad w_{fv}(x, t) = \sum_{i=1}^{\infty} W_i(x) T_i(t). \quad (8)$$

211 The solution for the normal mode [15][34] is

$$212 \quad W_i(x) = \sqrt{1/(\rho A a)} \phi_i(x), \quad (9)$$

213 where  $\phi_i(x)$  is the mode shape given as

$$214 \quad \phi_i(x) = \cosh(\beta_i x) - \cos(\beta_i x) - \sigma_i [\sinh(\beta_i x) - \sin(\beta_i x)]. \quad (10)$$

215 In Eq. (10),  $\beta_i$  is the wavenumber, obtained by  $\tan(\lambda_i) - \tanh(\lambda_i) = 0$  (frequency equation)  
 216 with  $\lambda_i = \beta_i a$ ; and  $\sigma_i = [\cosh(\lambda_i) - \cos(\lambda_i)] / [\sinh(\lambda_i) - \sin(\lambda_i)]$ . The solution for the  
 217 frequency equation  $\lambda_i$  and the value for  $\sigma_i$  are given in Appendix A.

218 As for the modal displacement  $T_i(t)$ , its governing equation is obtained by combining  
 219 Eqs. (4) and (8) and introducing the  $i$ th mode's natural frequency  $\omega_i = \beta_i^2 \sqrt{EI/(\rho A)}$  as

$$220 \quad T_i(t) = T_i(0) \cos(\omega_i t) + \frac{\dot{T}_i(0)}{\omega_i} \sin(\omega_i t), \quad (11)$$

221 where  $T_i(0)$  and  $\dot{T}_i(0)$  are the initial modal displacement and velocity, respectively.  
 222 According to [33], they can be determined from the initial displacement  $w_{fv}(x, 0)$  and the  
 223 velocity  $\dot{w}_{fv}(x, 0)$  of the free-vibration component, respectively, as

$$224 \quad T_i(0) = \int_0^a \rho A W_i(x) w_{fv}(x, 0) dx, \quad (12)$$

$$225 \quad \dot{T}_i(0) = \int_0^a \rho A W_i(x) \dot{w}_{fv}(x, 0) dx. \quad (13)$$

226 In Eq. (1), by setting  $t = 0$  with  $w(x, 0) = w_1 P(x)$  and  $\dot{w}(x, 0) = 0$ , the initial displacement  
 227 and velocity of free vibration are found to be

$$228 \quad w_{fv}(x, 0) = -F_0(x), \quad (14)$$

$$229 \quad \dot{w}_{iv}(x, 0) = -c_1 F_1(x) - \sum_{m=1}^M d_m \theta_m H_m(x). \quad (15)$$

230 Note that determination of  $T_i(0)$  and  $\dot{T}_i(0)$  via Eqs. (12), (13), (14) and (15) requires the  
231 solutions for shifting functions  $F_n(x)$  and  $H_m(x)$  (given in Sections 2.1.3 and 2.1.4).

### 232 2.1.3. Solutions for shifting functions for polynomials

233 The shifting functions for  $F_n(x)$  by solving the ordinary differential equation Eq. (6)  
234 together with the available boundary conditions (Supplementary file). Examination of Eq. (6)  
235 reveals  $F_N^{(4)}(x) = 0$ ,  $F_{N-1}^{(4)}(x) = 0$ , and  $EIF_{n-2}^{(4)}(x)c_{n-2} + \rho An(n-1)F_n(x)c_n = 0$  for  
236  $2 \leq n \leq N-2$  ( $c_0 = 1$ ). Therefore, the solutions for  $F_{N-1}^{(4)}(x)$  and  $F_N^{(4)}(x)$  are

$$237 \quad F_N(x) = -\frac{1}{2a^3}x^3 + \frac{3}{2a^2}x^2, \quad (16)$$

$$238 \quad F_{N-1}(x) = -\frac{1}{2a^3}x^3 + \frac{3}{2a^2}x^2. \quad (17)$$

239 And for  $F_n(x)$  ( $2 \leq n \leq N-2$ ) can be obtained by solving Eq. (6) iteratively.

240 For the case of  $N=3$ , for instance, the solutions of the shifting functions for the applied  
241 polynomial-displacement component are

$$242 \quad \begin{cases} F_3(x) = F_2(x) = -\frac{1}{2a^3}x^3 + \frac{3}{2a^2}x^2, \\ F_1(x) = -\frac{1}{1680a^3} \left[ k_1 x^7 - 7k_1 a x^6 + (39k_1 a^4 + 840)x^3 - (33k_1 a^5 + 2520a)x^2 \right], \\ F_0(x) = -\frac{k_0}{1680a^3} (x^7 - 7ax^6 + 39a^4 x^3 - 33a^5 x^2), \end{cases} \quad (18)$$

243 where  $k_1 = -6c_3 \rho A / (c_1 EI)$  and  $k_0 = -2c_2 \rho A / (c_0 EI)$ . The solutions for  $N=1$ ,  $N=2$  and  
244  $N=4$  are given in Supplementary file.

### 245 2.1.4. Solutions for shifting functions for harmonics

246 The shifting functions for  $H_m(x)$  are obtained by solving the differential equation Eq. (7)  
247 together with the boundary conditions (Supplementary file).

$$\begin{aligned}
248 \quad H_m(x) &= \frac{[\sin(\gamma_m a) + \sinh(\gamma_m a)]}{2[\cos(\gamma_m a) \sinh(\gamma_m a) - \cosh(\gamma_m a) \sin(\gamma_m a)]} \\
&\quad \left\{ -\cosh(\gamma_m x) + \cos(\gamma_m x) + \frac{\cos(\gamma_m a) + \cosh(\gamma_m a)}{\sin(\gamma_m a) + \sinh(\gamma_m a)} [\sinh(\gamma_m x) - \sin(\gamma_m x)] \right\}, \quad (19)
\end{aligned}$$

249 where  $\gamma_m^4 = \theta_m^2 \rho A / (EI)$ .

250 The combined results from Sections 2.1.1 to 2.1.4 give the deflection of the DCB arm  
 251 (shown in Fig. 1b) in Eq. (3) as

$$\begin{aligned}
252 \quad w(x, t) &= \frac{1}{a} \sum_{i=1}^{\infty} \phi_i(x) \left\{ \begin{aligned} & -\int_0^a \phi_i(x) F_0(x) dx \cos(\omega_i t) \\ & + \frac{1}{\omega_i} \left[ -c_1 \int_0^a \phi_i(x) F_1(x) dx + \beta_i^3 \Lambda_i \sum_{m=1}^M \frac{\theta_m d_m}{(\beta_i^4 - \gamma_m^4)} \right] \sin(\omega_i t) \end{aligned} \right\} \quad (20) \\
&\quad + P(x) w_1 + F_0(x) + \sum_{n=1}^N F_n(x) c_n t^n + \sum_{m=1}^M H_m(x) d_m \sin(\theta_m t),
\end{aligned}$$

253 where  $\Lambda_i = [(-1)^i \sqrt{\sigma_i^2 + 1} + \sqrt{\sigma_i^2 - 1}]$  (values given in Appendix A). The derivation of the  
 254 integral  $\int_0^a \phi_i(x) H_m(x) dx$ ,  $\int_0^a \phi_i(x) F_0(x) dx$  and  $\int_0^a \phi_i(x) F_1(x) dx$  are by partial integration  
 255 (details in Supplementary file).

256 As shown in Eq. (20), the total deflection is a combination of the free-vibration component  
 257 and extrapolations of the other general applied displacement components. For the applied  
 258 polynomial-displacement component, the 0th-order shifting function  $F_0(x)$  affects the initial  
 259 modal displacement of the free-vibration, while the first-order shifting function  $F_1(x)$  affects  
 260 the modal velocity; still, the other remaining shifting functions do not affect the free-vibration  
 261 component. For the applied harmonic-displacement component, its associated shifting  
 262 functions  $H_m(x)$  do not affect the modal displacement but affect the modal velocity.

## 263 2.2. Energy release rate

264 By combining Eqs. (2) and (20), the total dynamic ERR for the DCB specimen shown in  
 265 Fig. 1 is obtained as

$$266 \quad G = \frac{EI}{b} \left\{ \begin{array}{l} \left[ \begin{array}{l} -\beta_i^2 \int_0^a \phi_i(x) F_0(x) dx \cos(\omega_i t) \\ -\frac{c_1 \beta_i^2}{\omega_i} \int_0^a \phi_i(x) F_1(x) dx \sin(\omega_i t) \\ + \frac{\beta_i^5 \Lambda_i}{\omega_i} \sum_{m=1}^M \frac{\theta_m d_m}{(\beta_i^4 - \gamma_m^4)} \sin(\omega_i t) \end{array} \right] + \frac{3}{a^2} w_1 \\ + F_0^{(2)}(0) + \sum_{n=1}^N F_n^{(2)}(0) c_n t^n - \sum_{m=1}^M \frac{\gamma_m^2 d_m [\sinh(\gamma_m a) + \sin(\gamma_m a)]}{[\sinh(\gamma_m a) \cos(\gamma_m a) - \cosh(\gamma_m a) \sin(\gamma_m a)]} \sin(\theta_m t) \end{array} \right\}^2. \quad (21)$$

267 Note that Eq. (21) is for the general applied displacement with a combination of quasi-static,  
 268 polynomial and harmonic components; pragmatically, for a specific DCB test, the applied  
 269 displacement might be a component of  $w_0(t)$  in Eq. (1). For instance, under impact loads, the  
 270 displacement can be only polynomials. Under cyclic loads (conventional fatigue test) can only  
 271 be a combination of quasi-static displacement component determining the mean stress level  
 272 and one harmonic component determining the stress amplitude. Therefore, these two  
 273 immediate applications are investigated in detail in Section 2.2.1 for impact and in  
 274 Section 2.2.2 for fatigue.

275

### 276 2.2.1. ERR solution for DCB under impact loads

277 Generally, the displacement at the free end of one DCB arm under impact loads, such as  
 278 drop weight or split Hopkinson bar, can be obtained with a high-speed camera or by measuring  
 279 of the incident and reflected strain waves [21]. Once this displacement is obtained, it can be  
 280 fitted into polynomials, and by resorting to Eq. (21), the ERR can be determined. Assuming that  
 281 the impact loads are applied to the undeformed DCB with a zero initial displacement, that is,  
 282  $w_1 = 0$  in Eq. (1), and free-end displacement of one DCB arm can be fitted into the 3rd order-  
 283 polynomial, i.e.  $N = 3$  as a case of Eq. (3):

$$284 \quad w_0(t) = c_1 t + c_2 t^2 + c_3 t^3. \quad (22)$$

285 Then, by substituting Eqs. (18) and (22) into the general solution (Eq. (21)), and by regrouping

$$286 \quad \text{the relevant terms, the dynamic ERR is then } G = \frac{9EI}{ba^4} [w_0(t) + Q(t)]^2, \quad (23)$$

287 where  $Q(t)$  is induced displacement by the structural dynamic response:

$$\begin{aligned}
288 \quad Q(t) = & -\frac{4}{3}c_2a^4 \frac{\rho A}{EI} \sum_{i=1}^{\infty} \frac{\Lambda_i}{\lambda_i^3} \cos(\omega_i t) + \frac{2}{3}c_1a^2 \sqrt{\frac{\rho A}{EI}} \sum_{i=1}^{\infty} \frac{\Lambda_i}{\lambda_i} \sin(\omega_i t) \\
& -4c_3a^6 \frac{\rho A}{EI} \sqrt{\frac{\rho A}{EI}} \sum_{i=1}^{\infty} \frac{\Lambda_i}{\lambda_i^5} \sin(\omega_i t) - \frac{11}{420}c_2a^4 \frac{\rho A}{EI} - \frac{11}{140}c_3a^4 \frac{\rho A}{EI}t.
\end{aligned} \tag{24}$$

289 Note that when determining the dynamic ERR in Eq. (23), the total response of one DCB arm  
290 is considered, which includes the applied displacement  $w_0(t)$  and induced displacement  $Q(t)$   
291 due to structural vibration caused by the inertial effect. Also note that the total ERR in Eq. (23)  
292 includes the ERR components from the applied displacement  $w_0(t)$  and the induced  
293 displacement  $Q(t)$  as well as their coupling. The quasi-static component of the ERR (or strain  
294 ERR) can be determined by using the applied displacement  $w_0(t)$  directly in the quasi-static  
295 solution for the DCB, which gives the ERR component of quasi-static motion as

$$297 \quad G_{st}^U = \frac{9EIw_0^2(t)}{ba^4}. \tag{25}$$

298 Therefore, the total ERR in Eq. (23) can be written as a sum of quasi-static ERR  $G_{st}^U$  and  
299 dynamic ERR components  $G_{dyn}$  as

$$301 \quad G = G_{st}^U + G_{dyn}, \tag{26}$$

302 where

$$303 \quad G_{dyn} = \frac{9EI}{ba^4} [2w_0(t)Q(t) + Q^2(t)], \tag{27}$$

304 and, therefore, the dynamic factor can be defined as

$$305 \quad f_{dyn} = \frac{G_{dyn}}{G_{st}^U} = 2 \frac{Q(t)}{w_0(t)} + \left[ \frac{Q(t)}{w_0(t)} \right]^2. \tag{28}$$

306 Note that Eq. (27) represents all the dynamic effects, that is, the induced displacement and its  
307 coupling with the applied displacement. Specifically, these dynamic effects are: (1) inertia-  
308 induced local vibration, represented by terms with  $\sin(\omega_i t)$ , and (2) coupling between the local  
309 vibration and applied displacement, represented by terms with the product of  $w_0(t)\sin(\omega_i t)$ .  
310 However, in Eq. (24), interestingly, there are two terms of  $-11\rho Ac_2a^4/(420EI)$  and

311  $-11c_3a^4\rho At/(140EI)$  not related to the above two sources, and the close examination shows  
 312 that they come from the shifting function  $F_1(x)$ , which is solved by Eq. (6) that the solution  
 313 of  $F_1(x)$  depends on the solution of  $F_3(x)$ . This shows a nonlinear relationship between  
 314 shifting  $F_n(x)$  and the solutions for  $F_n(x)$  causes the motion coupling of the applied  
 315 displacement when the ERR is determined. And, therefore, this identifies the third dynamic-  
 316 effect source, which is the motion coupling of the applied polynomial displacement itself. It is  
 317 also worth noting that for the applied displacement of form  $w_0(t) = vt$  (setting  $c_1 = v$  being  
 318 the constant opening rate), that is, the DCB under constant high loading rate, the ERR is

$$319 \quad G = \frac{9EIv^2t^2}{ba^4} + \frac{12\sqrt{\rho AEI}v^2t}{ba^2} \sum_{i=1}^{\infty} \frac{\Lambda_i}{\lambda_i} \sin(\omega_i t) + \frac{4\rho Av^2}{b} \left[ \sum_{i=1}^{\infty} \frac{\Lambda_i}{\lambda_i} \sin(\omega_i t) \right]^2, \quad (29)$$

320 which coincides with [16].

### 321 2.2.2. ERR solution for DCB under cyclic loads

322 The general solution for the ERR in Eq. (21) can also be applied to the fatigue under cyclic  
 323 loads. Following the conventional method in ASTM D6115 [24], that is, applying a cyclic  
 324 displacement with the maximum value  $\delta_{\max}$  and the minimum value  $\delta_{\min}$ , the applied  
 325 displacement is

326

$$327 \quad w(t) = w_1 + d \sin(\theta t), \quad (30)$$

328 where  $w_1 = (\delta_{\max} + \delta_{\min})/2$  is the half mean applied amplitude,  $d = (\delta_{\max} - \delta_{\min})/2$  is the half  
 329 range or amplitude,  $\theta = 2\pi f$  is the angular frequency with  $f$  being the applied frequency.

330 Note that  $\delta_{\max}$  and  $\delta_{\min}$  are for one DCB arm measured from the symmetry line. Taking these  
 331 into Eq. (21), the ERR for this fatigue cyclic displacement load is

332

$$333 \quad G = \frac{9EI\delta_{\max}^2}{ba^4} \left[ \xi_{\text{mean}} + \xi_{\text{range}} \sin(\theta t) + \sum_{i=1}^{\infty} \xi_i \sin(\omega_i t) \right]^2, \quad (31)$$

334 where

$$335 \quad \xi_{\text{mean}} = \frac{1}{2}(1 + R), \quad (32)$$

$$\xi_{\text{range}} = -\frac{1}{6}(1-R) \frac{\gamma^2 a^2 [\sinh(\gamma a) + \sin(\gamma a)]}{[\sinh(\gamma a) \cos(\gamma a) - \cosh(\gamma a) \sin(\gamma a)]}, \quad (33)$$

$$\xi_i = \frac{1}{3}(1-R) \frac{\lambda_i^3 \Lambda_i \gamma^2 a^2}{(\lambda_i^4 - \gamma^4 a^4)}, \quad (34)$$

are the contributions to the total ERR from the mean load, the load range and the  $i$ th induced vibration, respectively, with  $R = \delta_{\min}/\delta_{\max}$  being the cyclic load ratio.

Note that the advantages of Eq. (31) allow to determine the fatigue delamination driving force, i.e.  $G_{\max}$  under the maximum load, without the need of measuring the applied loads as required by ASTM D6115. This is especially significant for high-frequency cyclic displacements, where the applied loads oscillate considerably and are very hard to measure.

A close examination of  $\xi_{\text{range}}/(1-R)$  and  $\xi_i/(1-R)$  reveals that they are both dimensionless and functions only of dimensionless parameter  $\gamma a$  (note that  $\gamma$  represents the applied frequency and structural property for  $\gamma^4 = 4\pi^2 f^2 \rho A/(EI)$ ). They are plotted versus  $\gamma a$  in Figs. 2 and 3 to illustrate their properties.

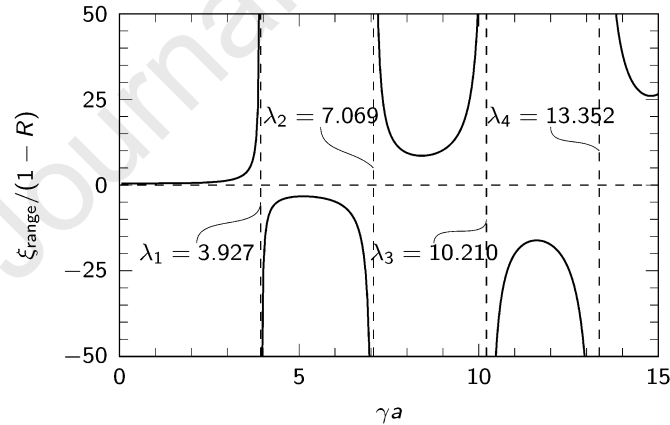
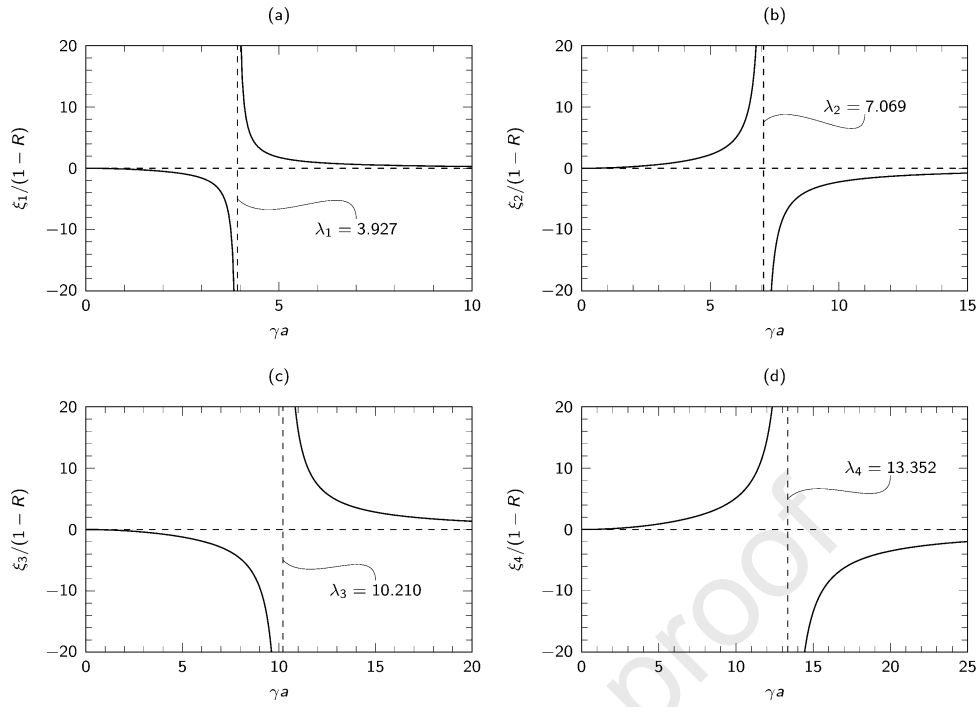


Fig. 2. Contribution to total ERR from applied cyclic loads

It is seen that the values of  $\xi_{\text{range}}/(1-R)$  and  $\xi_i/(1-R)$  remain relatively small when  $\gamma a$  is not in the vicinity of the eigenvalues  $\lambda_i$ ; otherwise, the beam system would go resonant giving an infinite value for ERR as the material fails immediately.



353

354

Fig. 3. Contribution to total ERR from  $i$ th induced free vibration

355

356

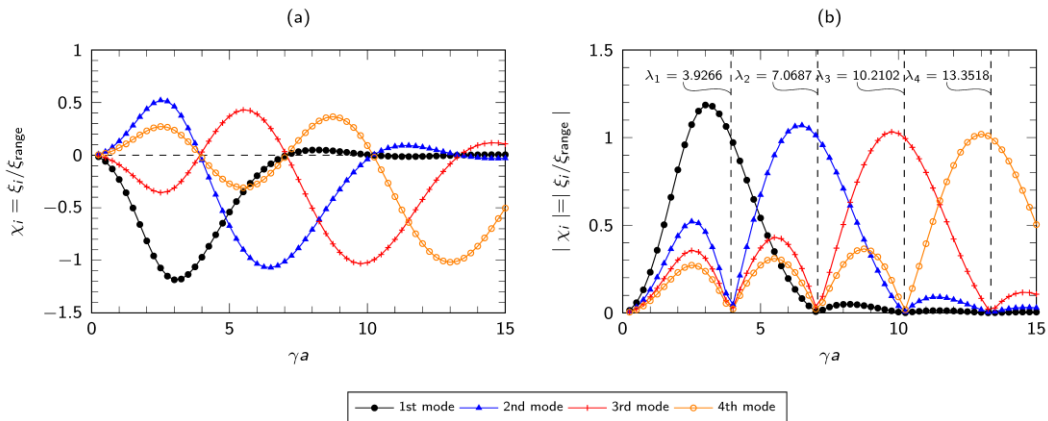
357

358

Note that the induced vibration contributions  $\xi_i$  are from the applied cyclic displacement range  $\xi_{\text{range}}$ , and, therefore, it is important to investigate the ratio between them to demonstrate the contribution from the applied cyclic displacement to the induced vibration as the relative dynamic effect.  $\chi_i$  is defined as

359

$$\chi_i = \frac{\xi_i}{\xi_{\text{range}}} = -\frac{2\lambda_i^3 \Lambda_i [\sinh(\gamma a) \cos(\gamma a) - \cosh(\gamma a) \sin(\gamma a)]}{(\lambda_i^4 - \gamma^4 a^4) [\sinh(\gamma a) + \sin(\gamma a)]}. \quad (35)$$



360

361

362

Fig. 4. (a) Vibration-induced dynamic factors; (b) absolute value of vibration-induced dynamic factors

363 Fig. 4 shows the relationship between  $\xi_i$  and  $\xi_{\text{range}}$  for a range of  $\gamma a$  values. For the first  
 364 vibration mode,  $\chi_1$  increases with  $\gamma a$  to a peak value of approximate 1.4, demonstrating the  
 365 maximum dynamic response is  $\xi_1 = 1.4\xi_{\text{range}}$ ; then  $\chi_1$  drops steadily to zero. However, the  
 366 interpretation of this should be based on the real composite material, considering a less stiff  
 367 CFRP with the longitudinal modulus of 10 GPa, density of 1000 kg m<sup>-3</sup>, and DCB with  
 368  $h = 1.5$  mm and  $a = 125$  mm (limiting geometry in ASTM D5528), the applied frequency of  
 369 100 Hz, which gives  $\gamma a = a\sqrt{4\pi^2 f^2 \rho A / (EI)} = 2.67$ ; to increase the applied frequency further  
 370 seems impossible due to the limitation of available experimental systems [27]. Therefore, in a  
 371 realistic case, the value of  $\gamma a$  might be well below 5, where the relative dynamic factor  $\chi_i$   
 372 decreases with increasing vibration-mode number, and the first vibration mode makes the  
 373 largest contribution compared with those of other vibration modes.

374 Another approach to study the induced dynamic contribution to the total ERR is by  
 375 investigating the absolute values, that is, the applied ERR component  $G_{\text{appl}}$  and vibration  
 376 induced ERR component  $G_{\text{dyn}}$  by expanding the Eq. (31) to have

$$377 \quad G = G_{\text{appl}} + G_{\text{dyn}}, \quad (36)$$

378 where

$$379 \quad G_{\text{appl}} = \frac{9EI\delta_{\text{max}}^2}{ba^4} \left[ \xi_{\text{mean}} + \xi_{\text{range}} \sin(\theta t) \right]^2, \quad (37)$$

$$380 \quad G_{\text{dyn}} = \frac{9EI\delta_{\text{max}}^2}{ba^4} \left\{ 2 \left[ \xi_{\text{mean}} + \xi_{\text{range}} \sin(\theta t) \right] \sum_{i=1}^{\infty} \xi_i \sin(\omega_i t) + \left[ \sum_{i=1}^{\infty} \xi_i \sin(\omega_i t) \right]^2 \right\}, \quad (38)$$

381 and, therefore, the dynamic factor can be defined as

$$382 \quad f_{\text{dyn}} = \frac{G_{\text{dyn}}}{G_{\text{appl}}} = \frac{2 \left[ \xi_{\text{mean}} + \xi_{\text{range}} \sin(\theta t) \right] \sum_{i=1}^{\infty} \xi_i \sin(\omega_i t) + \left[ \sum_{i=1}^{\infty} \xi_i \sin(\omega_i t) \right]^2}{\left[ \xi_{\text{mean}} + \xi_{\text{range}} \sin(\theta t) \right]^2}. \quad (39)$$

383 Note that Eqs. (31) to (39) are for the ERR time response: for its application to study fatigue  
 384 delamination initiation and propagation, the range or the maximum value of the ERR should  
 385 be used, and they are denoted  $G_{\text{max}}$ ,  $G_{\text{appl,max}}$  and  $G_{\text{dyn,max}}$ , respectively, for the maximum value  
 386 of Eqs. (36), (37) and (38).

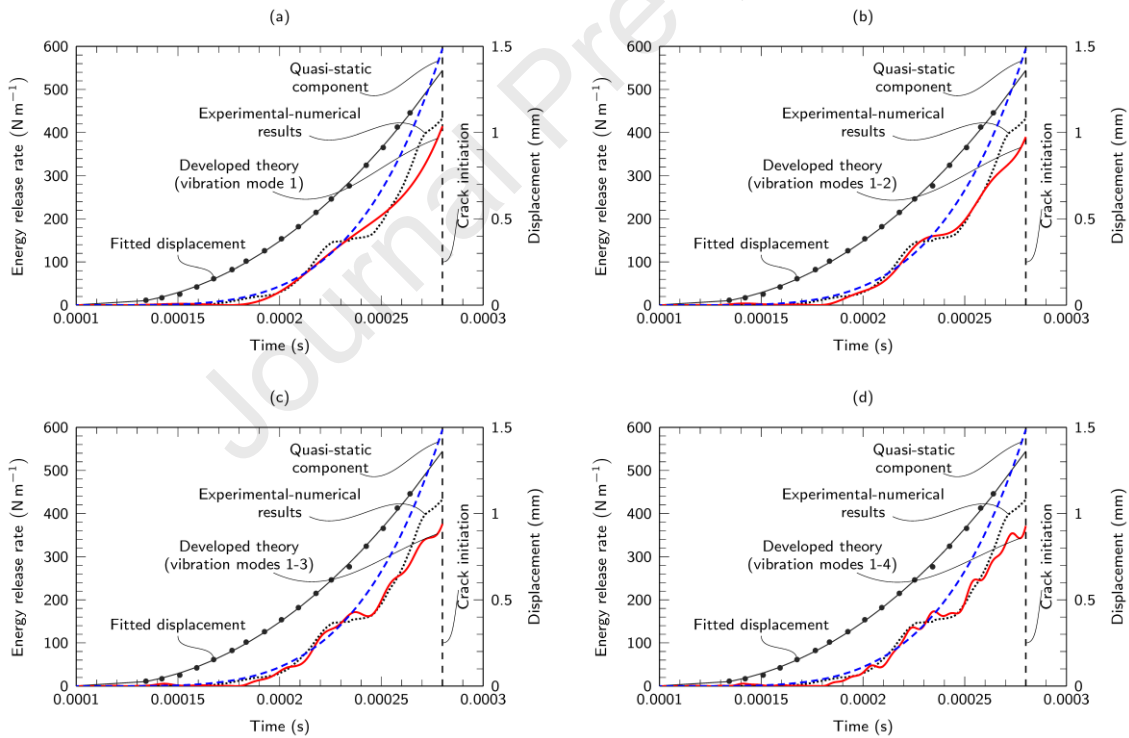
### 387 3. Applications and verifications

#### 388 3.1. DCB under split Hopkinson bar impact

389 To demonstrate and to verify the applications of the developed theory for impact, the  
 390 experimental data of the DCB of unidirectional CFRP specimens manufactured from the  
 391 T700/MTM28-1 prepreg in the split Hopkinson bar impact test from [21] is used. The  
 392 displacement curve was adopted from [21] and fitted into a third-order displacement curve:

$$393 \quad w_0(t) = 2.625 \times 10^{10} (t - t_0)^3 + 4.065 \times 10^7 (t - t_0)^2 - 7.885 \times 10^2 (t - t_0) \quad R^2 = 0.999, \quad (40)$$

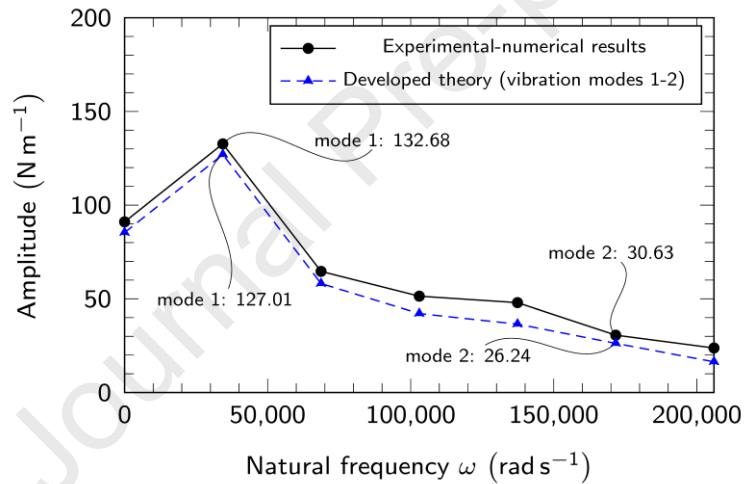
394 where  $t_0 = 9.8 \times 10^{-5}$  s is the estimated time for the DCB arm to start to deflect at the arrival of  
 395 incident wave as shown in Fig. 5a in [21]. Then it was substituted in Eq. (23) to determine the  
 396 dynamic ERR  $G$  that is compared with experimental-numerical solution from [21] in Fig. 5 for  
 397 a number of different vibration modes.



398  
 399 Fig. 5. Dynamic ERR versus time results from developed theory with first (a), first two (b),  
 400 first three (c), and first four (d) vibration modes together with dynamic ERR data from  
 401 experimental-numerical results for CFRP specimens of unidirectional stacking sequence

402 Fig. 5 shows an excellent agreement between the analytical solution and the experimental-  
 403 numerical results until crack-initiation time determined experimentally in [21] and the  
 404 analytical solution captures the oscillating nature of the ERR. The analytical solution with the

405 first vibration mode gives a mean value of the total ERR as shown in Fig. 5a. By adding the  
 406 second vibration mode (Fig. 5b), the analytical solution approaches the experimental-  
 407 numerical results. With addition of the third (Fig. 5c) and fourth (Fig. 5d) vibration modes, the  
 408 analytical solution becomes more oscillatory around the mean value of the first vibration mode.  
 409 This may be due to different formations: the analytical solution is based on the 1D plane-strain  
 410 condition using a longitudinal modulus, whereas the experimental-numerical result was  
 411 derived from a 2D finite-element-method (FEM) simulation with an orthotropic material  
 412 properties [21]. Still, the difference between the analytical solution and the experimental-  
 413 numerical result is insignificant. Note that the value of the dynamic ERR  $G$  is very small at the  
 414 initial stage at the arrival of incident wave, and before 0.00018 s, the  $G$  value approaches to  
 415 zero while the quasi-static component  $G_{st}^U$  increases with time. This is due to the negative  
 416 effect of ERR component due to dynamic effect  $G_{dyn}$ , which is further examined in Fig. 7.

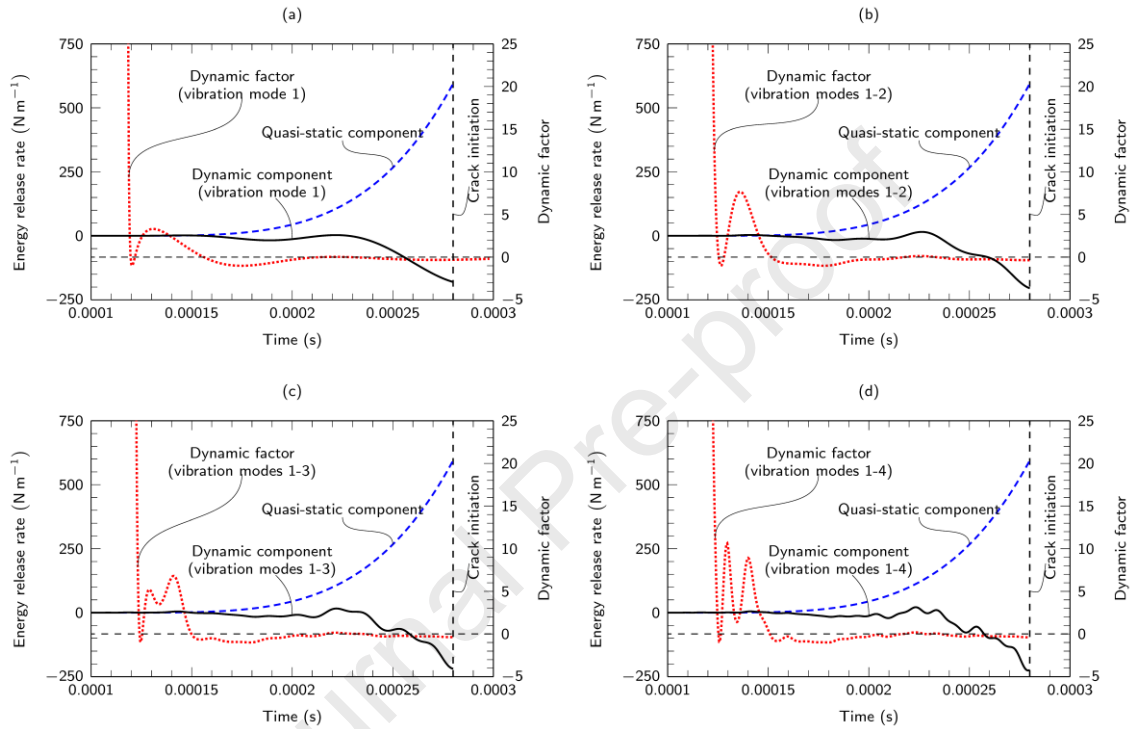


417  
 418 Fig. 6 Comparison of FFT results for experimental-numerical method and developed theory  
 419 for first two vibration modes

420 The agreement between the prediction of the developed theory and experimental-numerical  
 421 results can also be demonstrated with the Fast Fourier Transform (FFT) that provides a  
 422 quantitative assessment (Fig. 6). According to this, the contribution of the first vibration mode  
 423 in experimental-numerical results is 132.68 N m<sup>-1</sup>, while the respective theoretical result is  
 424 127.01 N m<sup>-1</sup>, with the error of -4.27%; for the second vibration mode, this error is -14.33%.

425 It is worth noting that the quasi-static solution is also plotted in Fig. 7 for comparison, and  
 426 it seems that the dynamic effect lowered the total ERR and postponed the crack initiation. To  
 427 further investigate the process, the ERR's quasi-static component  $G_{st}^U$  (Eq. (25)), dynamic

428 component  $G_{\text{dyn}}$  (Eq. (26)) and dynamic factor  $f_{\text{dyn}}$  (Eq. (27)) were plotted (Fig. 7). Note that  
 429 the ERR component due to quasi-static motion  $G_{\text{st}}^{\text{U}}$  is also referred as the strain energy release  
 430 rate (SERR) that can be calculated with a conventional data-reduction method when dynamic  
 431 effect is not considered. The comparison between  $G_{\text{st}}^{\text{U}}$  and dynamic ERR  $G$  presented in this  
 432 study (Figs. 5 and 7) also demonstrates the significance of the dynamic effect.



433  
 434 Fig. 7. Time response of dynamic ERR components and corresponding dynamic factors for  
 435 first (a), first two (b), first three (c) and first four (d) vibration modes

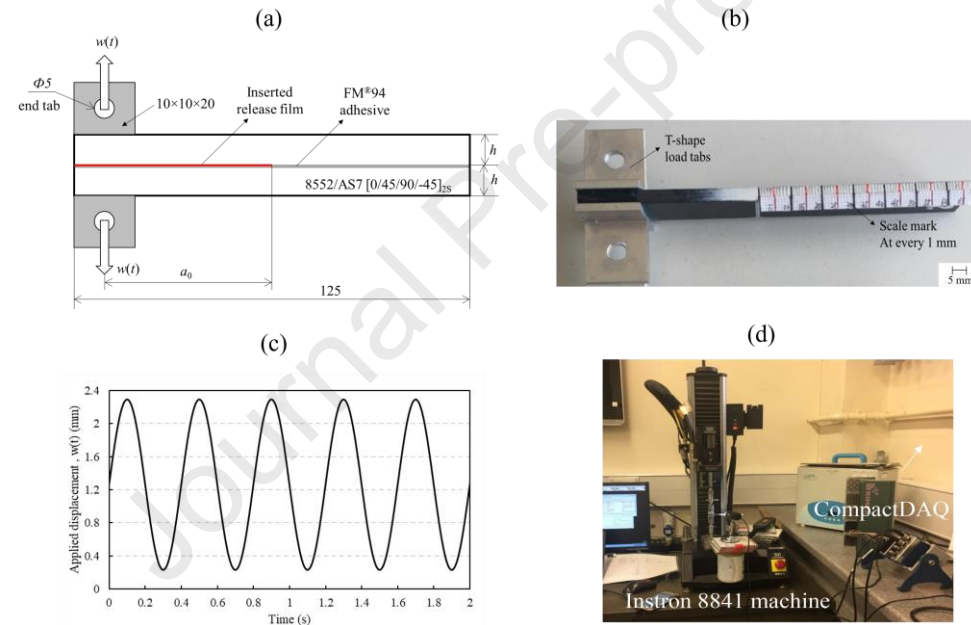
436 It is seen in Fig. 7 that the  $G_{\text{dyn}}$  actually increases initially and then decreases with time; and  
 437 this is due to the crack-tip motion that after the immediate impact the deflection around the  
 438 crack tip experiences an additional opening tendency giving positive  $G_{\text{dyn}}$  and  $f_{\text{dyn}}$ . After that,  
 439 due to the structural vibration and the associated reciprocating motion, the crack tip undergoes  
 440 closing and reduces the total ERR, resulting in negative  $G_{\text{dyn}}$  and  $f_{\text{dyn}}$ .

441 In general, the developed theory and the associated analytical solution for the split  
 442 Hopkinson bar impact provides an accurate prediction of the delamination driving force  
 443 compared with experimental-numerical methods, making it a powerful analytical tool to further  
 444 study the dynamic effect accompanied by the structural vibration, which the experimental-  
 445 numerical methods cannot achieve.

## 446 3.2. DCB under cyclic loads

## 447 3.2.1 Experimental verification

448 To confirm the applicability of the developed theory for fatigue delamination, in-house  
 449 fatigue experiments were conducted in accordance with ASTM D6115 (Fig. 8a) with a width  
 450 of 20 mm. Each cantilever beam was made of 16 plies of Hexply 8552/AS7 (density:  
 451  $1790 \text{ kg m}^{-3}$ ) CFRP in a quasi-isotropic layup of  $[0/45/90/-45]_{2s}$ , giving a thickness  $h = 2.2 \text{ mm}$ .  
 452 Two beams were bonded with FM94 adhesive. The elastic properties of the laminate and the  
 453 adhesive are given in Table 1. To monitor the delamination length, one side of the specimen  
 454 was painted with white spray and marked with a vernier height gauge at 1 mm interval  
 455 (Fig. 8b).



456  
 457 Fig. 8. (a) DCB specimen (units: mm); (b) specimen with end tabs and markings; (c) applied  
 458 cyclic displacement; (d) setup for fatigue test

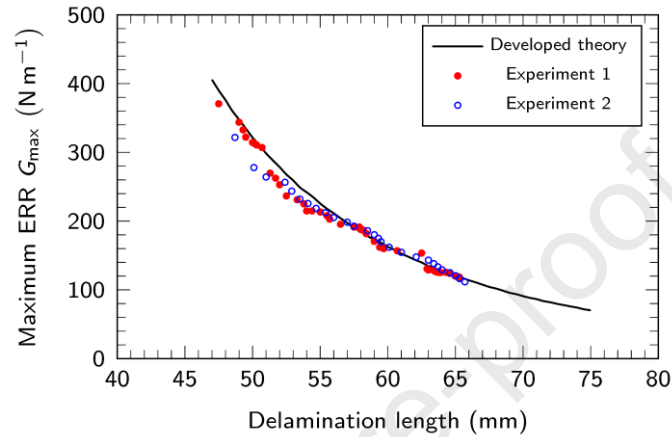
459 Table 1 Elastic properties of laminate and adhesives used in DCB specimens

Material	$E_1$ (GPa)	$E_2$ (GPa)	$G_{12}$ (GPa)	$\nu_{12}$
8552/AS7 laminate	56.42	56.42	21.64	0.30
FM94 adhesive	3	3	1.15	0.35

460

461 An Instron 8841 fatigue test machine (Fig. 8c) was used to provide displacement control  
 462 with the maximum displacement  $\delta_{\max} = 2.3 \text{ mm}$ ,  $R = 0.1$  and  $f = 5 \text{ Hz}$ . The applied loads were  
 463 measured and the maximum value  $P_{\max}$  for each delamination length is recorded. The

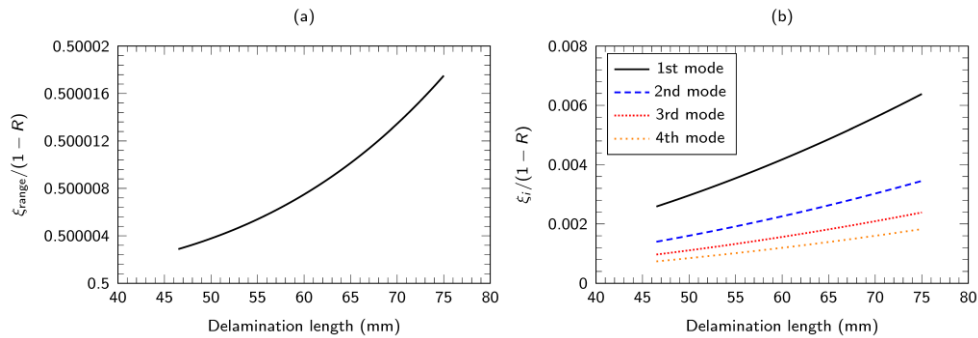
464 delamination length was measured when the test was paused at the maximum displacement.  
 465 According to ASTM D6115, the maximum ERR can be calculated via expression  
 466  $G_{\max} = (3P_{\max} \delta_{\max}) / [b(a + \Delta)]$  (where  $\delta_{\max}$  is for one DCB arm). This experimentally  
 467 determined maximum ERR value,  $G_{\max}$ , is then compared with the theoretical solution  
 468 (Eq. (31)) for various delamination lengths in Fig. 9.



469  
 470 Fig. 9. Dynamic mode-I ERR versus delamination length under maximum displacement

471 
$$\delta_{\max} = 2.3 \text{ mm } (R = 0.1, f = 5 \text{ Hz})$$

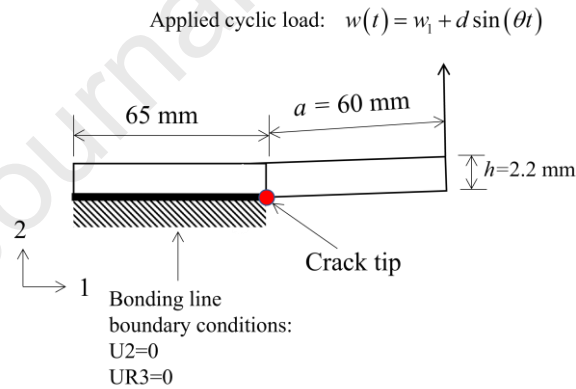
472 Fig. 9 shows that the analytical solution and experimental result are in excellent agreement,  
 473 but the analytical solution does not require the measurement of the applied load. To study the  
 474 influence of the vibration-induced dynamic effect, terms  $\xi_{\text{range}} / (1 - R)$  in Eq. (33) and  
 475  $\xi_i / (1 - R)$  in Eq. (34) were also plotted against the delamination length in Fig. 10.



476  
 477 Fig. 10. (a) Contribution to total ERR from applied cyclic loads; (b) contribution to total ERR  
 478 for induced vibration

## 479 3.2.2 Numerical verification

480 The influence of vibration-induced dynamic effect is very small (Fig. 10) and can be  
 481 neglected for the test frequency of 5 Hz. Still, the developed theory (Section 2.2.2) shows that  
 482 the dynamic effect increases with increasing applied frequency, and that the dynamic effect  
 483 can become significant. Note that, to apply higher frequencies, Maillet et al. [27] designed a  
 484 mechanical device capable of applying cyclic frequency up to 100 Hz. To demonstrate the  
 485 applicability of the theory in Section 2.2.2 and to investigate the induced dynamic effect, the  
 486 FEM was employed using a 2D model in Abaqus/Explicit with plane-strain elements (CPE4R).  
 487 Mechanical properties of 8552/AS7 laminate were employed in the finite-element model  
 488 according to an orthotropic elastic constitutive formulation in terms of engineering constants:  
 489  $E_1 = E_2 = 56.42$  GPa,  $E_3 = 10$  GPa,  $G_{13} = G_{23} = 10$  GPa,  $G_{12} = 21.64$  GPa,  $\nu_{12} = \nu_{23} = \nu_{13} = 0.30$ .  
 490 Due to the symmetry, one DCB arm was modelled with the boundary conditions and applied  
 491 displacement shown in Fig. 11. Small displacements were assumed. The mesh-convergence  
 492 study was conducted for uniform meshes of  $1 \times 1$  mm<sup>2</sup>,  $0.5 \times 0.5$  mm<sup>2</sup>,  $0.25 \times 0.25$  mm<sup>2</sup> and  
 493  $0.125 \times 0.125$  mm<sup>2</sup>, as shown in Fig. C1 in Appendix C, and the mesh of  $0.25 \times 0.25$  mm<sup>2</sup> was  
 494 chosen.

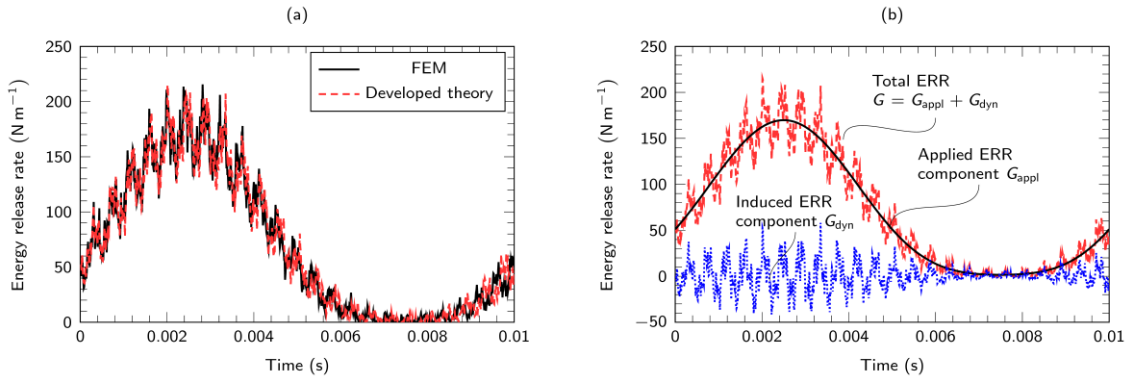


495

496

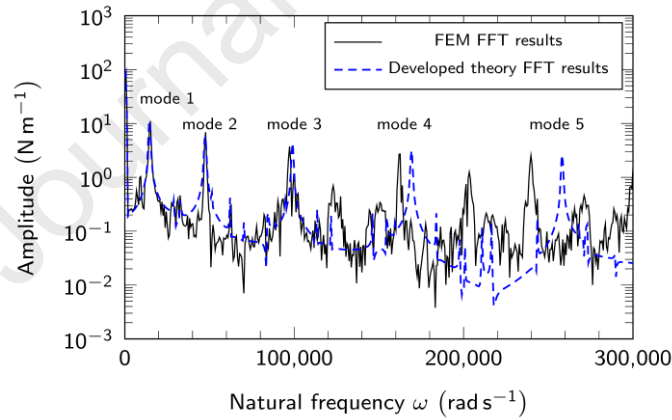
Fig. 11 Schematic of finite-element model and boundary conditions

497 For a uniform mesh of  $0.25 \times 0.25$  mm<sup>2</sup>, the ERR was determined with the virtual crack  
 498 closure technique (VCCT). For test frequency of 100 Hz and delamination length 60 mm, a  
 499 comparison of the analytical solution (Eq. (31)) and FEM are shown in Fig. 12a in terms of  
 500 ERR-time response.



501  
502 Fig. 12. (a) Comparison between developed theory and FEM; (b) partition of total ERR into  
503 applied and vibration-induced ERR components (test frequency 100 Hz)

504 An excellent agreement between the analytical solution and FEM is obvious in Fig. 12a,  
505 confirming that the induced vibration-related dynamic effect is significant for the frequency of  
506 100 Hz. A further examination of the ERR components in Fig. 12b using Eqs. (36), (37) and  
507 (38) demonstrates the absolute value of dynamic component with the maximum value of  
508 47.25 N m<sup>-1</sup> and the applied ERR component of 156.21 N m<sup>-1</sup>, giving a dynamic factor  $f_{\text{dyn}} =$   
509 30.24% according to Eq. (39). Therefore, the dynamic effect cannot be neglected.



510  
511 Fig. 13 Comparison of FFT results for FEM method and develop theory for first five  
512 vibration modes

513 In addition, the agreement between the developed theory and FEM simulation can be  
514 demonstrated by FFT analysis (Fig. 13). It is seen that first vibration mode makes the highest  
515 contribution to the total ERR. For the first three vibration modes, the frequencies are predicted  
516 accurately with the developed theory; quantitative comparison is given in Table 2.

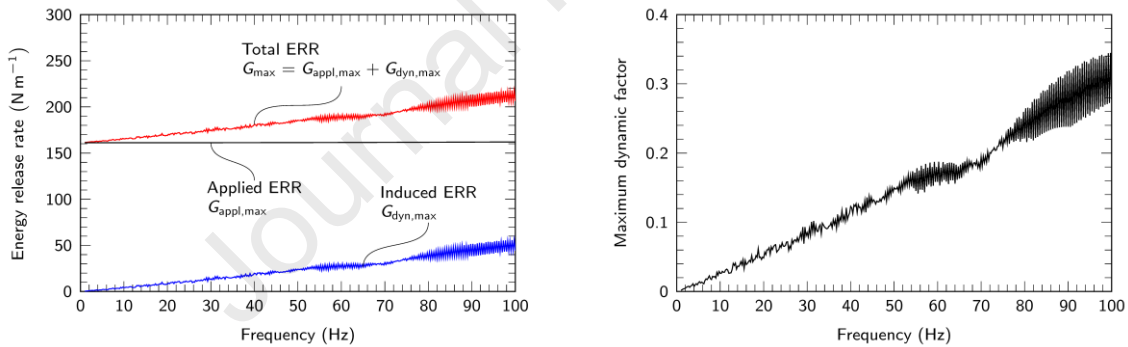
517 Table 2 Comparison of modal amplitudes and frequencies for FEM and developed theory

	Amplitude (N m <sup>-1</sup> )			Frequency (rad s <sup>-1</sup> )		
	FEM	Analytical	Error (%)	FEM	Analytical	Error (%)
Mode 1	11.06	11.34	-2.53	15064.58	14436.89	4.17
Mode 2	6.86	5.01	26.97	47704.50	47076.81	1.32
Mode 3	3.73	4.35	-16.62	97292.08	99175.15	-1.94
Mode 4	2.70	3.14	-16.30	162571.93	169476.53	-4.25
Mode 5	2.53	2.60	-2.77	239777.90	257980.94	-7.59

518

519 It is seen that the error (relative difference) for amplitude of first vibration mode predicted  
520 with the analytical solution and FEM result is -2.53%, although the respective values for the  
521 second and third vibration modes are larger.

522 To further study the test frequency effect,  $G_{\max}$  for the above case was calculated across a  
523 frequency range between 1 Hz and 100 Hz (Fig. 14). Evidently, the maximum applied ERR  
524  $G_{\text{appl,max}}$  (Eq. (37)) does not increase with the test frequency (Fig. 14a), but the maximum  
525 induced dynamic component  $G_{\text{dyn,max}}$  increases steadily with growing frequency.



526

527 Fig. 14. (a) Total ERR and its two components obtained at maximum applied displacement;

528

(b) dynamic factor at maximum applied displacement

529 The maximum dynamic factor calculated using Eq. (39) reaches the maximum value up  
530 to 34.5% in the studied frequency range (Fig. 14b), suggesting that the induced vibration-  
531 related dynamic effect must be taken into consideration when conducting high-frequency  
532 fatigue tests.

533 The verification with the FEM demonstrates the accuracy of the developed theory; hence,  
534 it can be used in both low- and high-frequency fatigue delamination. Additionally, the  
535 developed theory does not require measurement of the applied loads as the conventional  
536 method (ASTM D6115) requests; this is particularly attractive for higher-frequency tests,

537 where the applied force cannot be measured accurately because of the significant structural  
538 vibration.

#### 539 **4. Conclusion**

540 The total dynamic energy release rate (ERR) in the double cantilever beam (DCB) test under  
541 general applied displacement was derived analytically for the first time based on the structural  
542 vibration theory, allowing determination of the total ERR without measurement of the external  
543 force for arbitrary applied displacements. Two useful solutions are derived for two  
544 experimental techniques broadly used in analysis of composites: the split Hopkinson bar impact  
545 for assessment of the loading-rate effect on the delamination behavior and the cyclic loads for  
546 studying the fatigue delamination behavior.

547 For the DCB under Hopkinson bar impact, the total dynamic ERR can be derived and  
548 decomposed into the quasi-static and induced vibration-related components accounting for the  
549 total dynamic effect. A dynamic factor is defined for quantitative evaluation of the dynamic  
550 effect. The analytical solution was validated with the published experimental data showing an  
551 excellent agreement. The study also demonstrated the oscillating nature of the ERR caused by  
552 the opening and closing of the crack tip due to structural vibration.

553 For the DCB under cyclic loads, the total dynamic ERR can be decomposed into the applied  
554 ERR and vibration-induced components, and the relative dynamic effect and the total dynamic  
555 effects were defined. The analytical solution was validated by in-house fatigue delamination  
556 experiment with an excellent agreement until the crack initiation. The applicability for high-  
557 frequency cyclic loads was verified with the finite element method. It was found that  
558 dynamic effect increased with applied load frequency, and for a particular case of 100 Hz, the  
559 dynamic effect contributed up to 35.7% of the applied ERR, showing the significance of  
560 structural vibration.

561 The derived theory is readily applicable to various problems for evaluation of the dynamic  
562 mode-I delamination driving force with two immediate applications for measuring the dynamic  
563 fracture toughness and determining the fatigue-delamination-driving force as demonstrated in  
564 this study.

565 **Appendices**566 *Appendix A. Boundary conditions*567 The boundary conditions for the free-vibration component  $w_{fv}(x,t)$  and the shifting functions568  $F_n(x)$  and  $H_m(x)$  are presented in Table A.1569 Table A.1 Boundary conditions for  $w(x,t)$  and its components

Boundary	Total deflection $w(x,t)$	Free-vibration component $w_{fv}(x,t)$	Mode shape $\phi_i(x)$	Shifting functions $F_n(x)$		Shifting functions $H_m(x)$
				$n=0$	$n \geq 1$	
				$x=0$	$w(0,t)=0$	
	$w^{(1)}(0,t)=0$	$w_{fv}^{(1)}(0,t)=0$	$\phi_i^{(1)}(0)=0$	$F_0^{(1)}(0)=0$	$F_n^{(1)}(0)=0$	$H_m^{(1)}(0)=0$
$x=a$	$w(a,t)=w_0(t)$	$w_{fv}(a,t)=0$	$\phi_i(a)=0$	$F_0(a)=0$	$F_n(a)=1$	$H_m(a)=1$
	$w^{(2)}(a,t)=0$	$w_{fv}^{(2)}(a,t)=0$	$\phi_i^{(2)}(a)=0$	$F_0^{(2)}(a)=0$	$F_n^{(2)}(a)=0$	$H_m^{(2)}(a)=0$

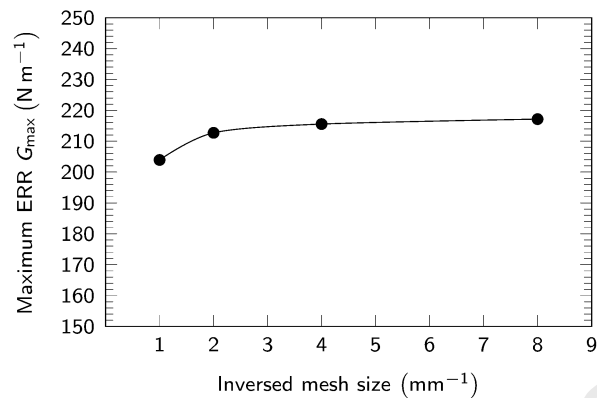
570

571 *Appendix B. Solution for frequency equation and relevant modal parameters*

572 Table B.1 Solution of frequency equation and relevant modal parameters

Mode number	$\lambda_i$	$\sigma_i$	$\Lambda_i$
1	3.92660231	1.000777304	-1.375327127
2	7.06858275	1.000001445	1.415914585
3	10.21017612	1.000000000	$-\sqrt{2}$
4	13.35176878	1.000000000	$\sqrt{2}$
5	16.49336143	1.000000000	$-\sqrt{2}$
$i > 5$	$(4i+1)\pi/4$	1.0	$(-1)^i \sqrt{2}$

573

574 *Appendix C. Results of mesh-size convergence study*

575

576

Fig. C1 Mesh-size convergence results

577

578 **Data availability**

579 The authors confirm that the data supporting the findings of this study are available within  
 580 the article.

581 **Acknowledgement**

582 This work was supported by the National Natural Science Foundation of China (Grant No.  
 583 51401028, No. 51271193, No. 11790292), the Strategic Priority Research Program of the  
 584 Chinese Academy of Sciences (Grant No. XDB22040303), and the Innovation Program  
 585 (237099000000170004).

586 **References**

- 587 [1] C. Soutis, "Carbon fiber reinforced plastics in aircraft construction," *Mater. Sci. Eng.*  
 588 *A*, vol. 412, no. 1–2, pp. 171–176, 2005, doi: 10.1016/J.MSEA.2005.08.064.
- 589 [2] C. González, J. J. Vilatela, J. M. Molina-Aldareguía, C. S. Lopes, and J. LLorca,  
 590 "Structural composites for multifunctional applications: Current challenges and future  
 591 trends," *Prog. Mater. Sci.*, vol. 89, pp. 194–251, 2017.
- 592 [3] T. A. Sebaey, N. Blanco, J. Costa, and C. S. Lopes, "Characterization of crack  
 593 propagation in mode I delamination of multidirectional CFRP laminates," *Compos.*  
 594 *Sci. Technol.*, vol. 72, no. 11, pp. 1251–1256, 2012.

- 595 [4] S. Ogihara and N. Takeda, "Interaction between transverse cracks and delamination  
596 during damage progress in CFRP cross-ply laminates," *Compos. Sci. Technol.*, vol. 54,  
597 no. 4, pp. 395–404, 1995.
- 598 [5] M. R. Wisnom, "The role of delamination in failure of fibre-reinforced composites,"  
599 *Philos. Trans. R. Soc. A Math. Phys. Eng. Sci.*, vol. 370, no. 1965, pp. 1850–1870,  
600 2012.
- 601 [6] X. Zhao, W. Chen, X. Han, Y. Zhao, and S. Du, "Enhancement of interlaminar fracture  
602 toughness in textile-reinforced epoxy composites with polyamide 6/graphene oxide  
603 interlaminar toughening tackifier," *Compos. Sci. Technol.*, vol. 191, pp. 108094, 2020.
- 604 [7] J. Zhang, T. Yang, T. Lin, and C. H. Wang, "Phase morphology of nanofibre  
605 interlayers: Critical factor for toughening carbon/epoxy composites," *Compos. Sci.  
606 Technol.*, vol. 72, no. 2, pp. 256–262, 2012.
- 607 [8] X. Sun, L. Tong, M. D. K. Wood, and Y. W. Mai, "Effect of stitch distribution on  
608 mode I delamination toughness of laminated DCB specimens," *Compos. Sci. Technol.*,  
609 vol. 64, no. 7–8, pp. 967–981, 2004.
- 610 [9] T. Yang, C. H. Wang, J. Zhang, S. He, and A. P. Mouritz, "Toughening and self-  
611 healing of epoxy matrix laminates using mendable polymer stitching," *Compos. Sci.  
612 Technol.*, vol. 72, no. 12, pp. 1396–1401, 2012.
- 613 [10] B. M'membe, M. Yasaei, S. R. Hallett, and I. K. Partridge, "Effective use of metallic  
614 Z-pins for composites' through-thickness reinforcement," *Compos. Sci. Technol.*, vol.  
615 175, 2018, pp. 77–84, 2019.
- 616 [11] S. Tang, S. Lemanski, X. Zhang, and D. Ayre, "Fatigue life prediction of z-fibre  
617 pinned composite laminate under mode I loading," *Compos. Sci. Technol.*, vol. 174,  
618 pp. 221–231, 2019.
- 619 [12] ASTM D5528, "Standard test method for mode I interlaminar fracture toughness of  
620 unidirectional fiber-reinforced polymer matrix composites," *ASTM International*.  
621 2014.
- 622 [13] M. May, "Measuring the rate-dependent mode I fracture toughness of composites - A  
623 review," *Compos. Part A Appl. Sci. Manuf.*, vol. 81, pp. 1–12, 2016.
- 624 [14] L.B.Freund, *Dynamic Fracture Mechanics*. Cambridge University Press, 1990.
- 625 [15] T. Chen, C. M. Harvey, S. Wang, and V. V. Silberschmidt, "Dynamic interfacial  
626 fracture of a double cantilever beam," *Eng. Fract. Mech.*, vol. 225, pp. 1–9, 2020.
- 627 [16] T. Chen, C. M. Harvey, S. Wang, and V. V Silberschmidt, "Delamination propagation  
628 under high loading rate," *Compos. Struct.*, vol. 253, pp. 112734, 2020.

- 629 [17] T. Chen, C. M. Harvey, S. Wang, and V. V. Silberschmidt, “Dynamic delamination on  
630 elastic interface,” *Compos. Struct.*, vol. 234, pp. 111670, 2020.
- 631 [18] G. Hug, P. Thévenet, J. Fitoussi, and D. Baptiste, “Effect of the loading rate on mode I  
632 interlaminar fracture toughness of laminated composites,” *Eng. Fract. Mech.*, vol. 73,  
633 no. 16, pp. 2456–2462, 2006.
- 634 [19] M. Colin de Verdiere, A. A. Skordos, A. C. Walton, and M. May, “Influence of  
635 loading rate on the delamination response of untufted and tufted carbon epoxy non-  
636 crimp fabric composites/Mode II,” *Eng. Fract. Mech.*, vol. 96, pp. 1–10, 2012.
- 637 [20] C. Sun and C. Han, “A method for testing interlaminar dynamic fracture toughness of  
638 polymeric composites,” *Compos. Part B Eng.*, vol. 35, no. 6–8, pp. 647–655, 2004.
- 639 [21] H. Liu, H. Nie, C. Zhang, and Y. Li, “Loading rate dependency of Mode I interlaminar  
640 fracture toughness for unidirectional composite laminates,” *Compos. Sci. Technol.*,  
641 vol. 167, pp. 215–223, 2018.
- 642 [22] C. Guo and C. T. Sun, “Dynamic mode-I crack-propagation in a carbon/epoxy  
643 composite,” *Compos. Sci. Technol.*, vol. 58, no. 9, pp. 1405–1410, 1998.
- 644 [23] P. Kumar and N. N. Kishore, “Initiation and propagation toughness of delamination  
645 crack under an impact load,” *J. Mech. Phys. Solids*, vol. 46, no. 10, pp. 1773–1787,  
646 1998.
- 647 [24] ASTM D 6115, “Standard Test Method for Mode I Fatigue Delamination Growth  
648 Onset of Unidirectional,” *ASTM International*. 2005.
- 649 [25] M. Hojo, S. Matsuda, M. Tanaka, S. Ochiai, and A. Murakami, “Mode I delamination  
650 fatigue properties of interlayer-toughened CF/epoxy laminates,” *Compos. Sci.*  
651 *Technol.*, vol. 66, no. 5, pp. 665–675, 2006.
- 652 [26] Y. Liu, X. Zhang, S. Lemanski, H. Y. Nezhad, and D. Ayre, “Experimental and  
653 numerical study of process-induced defects and their effect on fatigue debonding in  
654 composite joints,” *Int. J. Fatigue*, vol. 125, pp. 47–57, 2019.
- 655 [27] I. Maillet, L. Michel, G. Rico, M. Fressinet, and Y. Gourinat, “A new test  
656 methodology based on structural resonance for mode I fatigue delamination growth in  
657 an unidirectional composite,” *Compos. Struct.*, vol. 97, pp. 353–362, 2013.
- 658 [28] C. S. Lee, H. J. Kim, A. Amanov, J. H. Choo, Y. K. Kim, and I. S. Cho, “Investigation  
659 on very high cycle fatigue of PA66-GF30 GFRP based on fiber orientation,” *Compos.*  
660 *Sci. Technol.*, vol. 180, pp. 94–100, 2019.

- 661 [29] D. Backe, F. Balle, and D. Eifler, “Fatigue testing of CFRP in the Very High Cycle  
662 Fatigue (VHCF) regime at ultrasonic frequencies,” *Compos. Sci. Technol.*, vol. 106,  
663 pp. 93–99, 2015.
- 664 [30] S. Hashemi, A. J. Kinloch, and J. G. Williams, “Corrections needed in double-  
665 cantilever beam tests for assessing the interlaminar failure of fibre-composites,” *J.*  
666 *Mater. Sci. Lett.*, vol. 8, no. 2, pp. 125–129, 1989.
- 667 [31] T. Chen, C. M. Harvey, S. Wang, and V. V. Silberschmidt, “Analytical corrections for  
668 double-cantilever beam tests,” *Int. J. Fract.*, vol. 229, no. 2, pp. 269–276, 2021.
- 669 [32] D. A. Grant, “Beam vibrations with time-dependent boundary conditions,” *J. Sound*  
670 *Vib.*, vol. 89, no. 4, pp. 519–522, 1983.
- 671 [33] S. S. Rao, *Vibration of Continuous Systems*. John Wiley & Sons, 2007.
- 672 [34] R. D. Blevins, *Formulas for Natural Frequency and Mode Shape*. Van Nostrand  
673 Reinhold, 1979.
- 674

### **Highlights**

- > Analytical theory developed for mode-I dynamic energy release rate
- > Quasi-static, dynamic, and general cyclic loads solved analytically
- > Structural vibration included to account for dynamic effect
- > Dynamic effect studied and quantified with induced displacement
- > Finite-element-method simulation and in-house fatigue test verify the analytical theory

Journal Pre-proof

**Declaration of interests**

The authors declare that they have no known competing financial interests or personal relationships that could have appeared to influence the work reported in this paper.

The authors declare the following financial interests/personal relationships which may be considered as potential competing interests:

Journal Pre-proof